The Journal of Chemical Physics

RESEARCH ARTICLE | NOVEMBER 29 2023

Quantum-mechanical water-flow enhancement through a sub-nanometer carbon nanotube

Alberto Ambrosetti ; Pier Luigi Silvestrelli

J. Chem. Phys. 159, 204709 (2023)
https://doi.org/10.1063/5.0182711

The Journal of Chemical Physics ARTICLE pubs.aip.org/aip/jcp

Quantum-mechanical water-flow enhancement through a sub-nanometer carbon nanotube

Cite as: J. Chem. Phys. 159, 204709 (2023); doi: 10.1063/5.0182711
Submitted: 20 October 2023 • Accepted: 2 November 2023 •
Published Online: 29 November 2023

Alberto Ambrosetti[a] and Pier Luigi Silvestrelli

AFFILIATIONS

Dipartimento di Fisica e Astronomia, Università degli Studi di Padova, via Marzolo 8, 35131 Padova, Italy

[a]Author to whom correspondence should be addressed: alberto.ambrosetti@unipd.it

ABSTRACT

Experimental observations unambiguously reveal quasi-frictionless water flow through nanometer-scale carbon nanotubes (CNTs). Classical fluid mechanics is deemed unfit to describe this enhanced flow, and recent investigations indicated that quantum mechanics is required to interpret the extremely weak water–CNT friction. In fact, by quantum scattering, water can only release discrete energy upon excitation of electronic and phononic modes in the CNT. Here, we analyze in detail how a traveling water molecule couples to both plasmon and phonon excitations within a sub-nanometer, periodic CNT. We find that the water molecule needs to exceed a minimum speed threshold of ~50 m/s in order to scatter against CNT electronic and vibrational modes. Below this threshold, scattering is suppressed, as in standard superfluidity mechanisms. The scattering rates, relevant for faster water molecules, are also estimated.

I. INTRODUCTION

Macroscale fluid-mechanics[1] associates higher flow-resistance with water passing through narrower tubes by virtue of enhanced interface friction effects. However, when nm scales are approached, striking deviations from macroscopic laws arise and ordered low-dimensional water arrangements[2–4] can emerge. Surprisingly, high water-flow rates were repeatedly measured[5–7] in carbon nanotubes (CNTs), and a steep permeability increase[8] was detected when decreasing CNT radii. Already at the ~10 nm scale, measured permeabilities can exceed no-slip Haagen–Poiseuille[8–10] predictions by two orders of magnitude, and discrepancies rapidly increase at even smaller radii.

From a technological point of view, robust nanoscale enhanced flow promises transformative impact in nanofluidics and selective fluid transport. Energy-efficient water filtration[11] was proposed based on CNT membranes, which could provide an ideal means for the increasingly relevant issue of water purification/desalinization.[12]

Semi-classical molecular dynamics simulations could predict[4,9,10,13,14] finite permeability enhancement at lower radii,[4,9,10,13,14] which was attributed to curvature-dependent incommensurateness[4] between confined water and the CNT lattice or to the collective burst motion[13] of water molecules in a single file. However, semi-classical permeabilities underestimate experimental values by several orders of magnitude and do not exhibit[8,10] the expected low-radius divergence. Quantum effects are thus expected to become increasingly relevant when CNT radii approach the nm scale, i.e., when lateral confinement is more pronounced.

Based on Fermi's golden rule, here we develop a truly quantum-mechanical theory for the scattering between a water molecule and both vibrational (phonons) and electronic (plasmon) modes of a (5,5) CNT. These scattering channels are assumed[15–17] to be responsible for the main friction mechanisms since they can transfer energy from water to the CNT. Shortly, if some energy is transferred from water to CNT plasmons or phonons, the kinetic energy of water diminishes, which determines an effective friction force.

II. METHODS AND PRELIMINARY INVESTIGATIONS

The (5,5) CNT has a radius of 3.41 Å and can accommodate a single water molecule in its section. In our previous work,[15] we determined the preferential configurations of single and multiple water molecules in the CNT. The single water molecule is preferentially located at the center of the CNT, with its dipole moment aligned with the CNT longitudinal axis (see Fig. 1). The stability of this configuration is attributed to the high polarizability anisotropy of the CNT.[15,18–20] By repeating this configuration along the CNT axis, one can accommodate multiple water molecules.

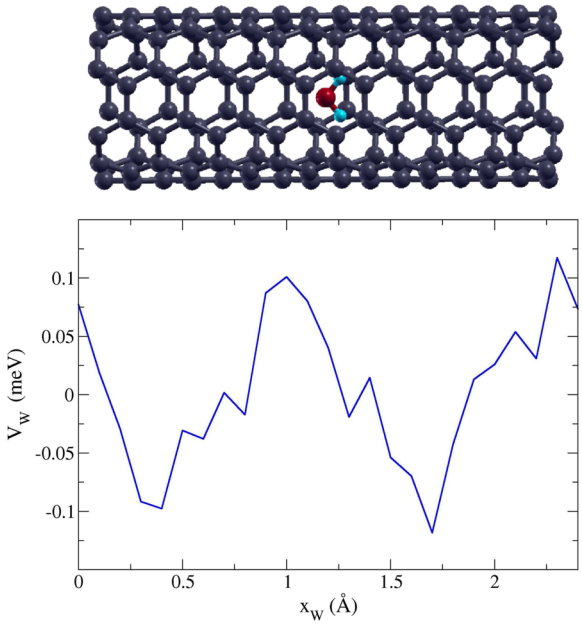

FIG. 1. Potential V_W computed at equilibrium ionic positions ($\bar{\mathbf{R}}_{ion}$) and in the absence of electronic displacements ($\delta\rho_{el} = 0$). The optimal configuration of a single water molecule confined in the (5,5) CNT is shown earlier. The water dipole is aligned with the CNT longitudinal axis. The green segment indicates the length of the CNT unit cell. The small irregularities of the potential (of the order of 10^{-2} meV) are attributed to the intrinsic convergence limits of the DFT calculation, while the main structure can be approximated by a sinusoidal function.

The efficiency of this configuration is due to the alignment of all dipoles, although water–water interactions are non-covalent; electrostatic and van der Waals forces determine water–water attraction. The configuration described so far is expected to largely contribute to water transport, especially in low density regimes. Hydrogen-bonded water pairs could form, but the energy gain of this configuration with respect to non-bonded dimers amounts to only 0.14 eV.[15] Moreover, long H-bonded chains were found to be unstable, suggesting again a preference for longitudinal-dipole arrangements.

As a preliminary investigation, we computed the energy landscape V_W of a water molecule moving along the CNT. First-principle calculations were performed within the density functional theory (DFT) framework, exploiting the Quantum Espresso[21] suite. A water monomer was introduced in a supercell containing eight replicas of the CNT unit cell (with a total length of 19.7 Å), and the energy was sampled by small consecutive displacements of the water molecule. The semi-local Perdew–Burke–Ernzerhof[22] functional was adopted, and van der Waals interactions[23] were accounted for by means of the many-body dispersion[24–26] (MBD) approach, thereby explicitly including collective polarization/depolarization effects at an effective random phase approximation (RPA) level. Pseudopotentials were introduced, and wavefunctions were expanded on a plane-wave basis set with an energy cutoff of 50 Ry, while a vacuum space of 15 Å was introduced between lateral CNT periodic replicas to minimize unwanted periodicity effects. The convergence of our calculations was thoroughly tested in our previous[15] work.

In the spirit of a perturbative theory, we focus on the motion of a single water molecule along the CNT. Our results are thus expected to be increasingly accurate at lower water densities. We approximate water as a pointlike particle coupled to the CNT. The Hamiltonian that describes the one-dimensional motion of water along the CNT is

$$H_W = -\frac{\partial^2_{x_W}}{2m_W} + V_W(x_W, \mathbf{R}_{ion}, \boldsymbol{\delta\rho}_{el}). \quad (1)$$

Here x_W and m_W are the longitudinal coordinates of water (along the CNT) and its mass, respectively, while the dependence of the potential energy V_W on CNT atom coordinates ($\mathbf{R}_{ion}$) and electronic charge variations ($\boldsymbol{\delta\rho}_{el}$) are explicited. We assume that the CNT longitudinal axis is aligned with the $\hat{x}$ axis, while the $\hat{y}, \hat{z}$ axes will be orthogonal to the CNT. In this expression, we implicitly adopted the Born–Oppenheimer approximation and identified the equilibrium charge distribution with that obtained by DFT. However, we underline that C atoms are free to move and electronic charges can be displaced (we will hereafter adopt a discretized model for charge hopping from one atomic site to another within the CNT).

III. SINGLE-PARTICLE WATER STATES

We diagonalize H_W with a frozen optimal configuration (i.e., zero atomic and charge displacements). Atomic units are adopted hereafter for simplicity. The potential energy is plotted in Fig. 1 as a function of x_W and can be well approximated by a sinusoidal function: $V_W(x_W) \sim V \sin((Q/2)x_W)$, where $Q = 2\pi/L$ and L is the CNT unit cell length (i.e., 2.46 Å). At the PBE + MBD level, one obtains $V \sim 0.1$ meV, i.e., the potential is extremely smooth. We note that the accurate account of many-body vdW effects by MBD diminishes the potential corrugation with respect to a pairwise vdW correction[15,27] (which predicts $V \sim 0.35$ meV). In fact, MBD is known to predict highly delocalized dipole fluctuations in low-dimensional nanosystems,[20,28] and this can smooth out the potential energy surface.

Numerical diagonalization is straightforward, and the single-particle energy eigenvalues are reported in Fig. 2 as a function of the wave-vector q within the first Brillouin zone (BZ). The spectrum does not differ much from that of a free particle except for irrelevant energy shifts and tiny gaps at the BZ edges. In practice, one could unfold the bands (letting q go beyond the BZ), obtaining a roughly parabolic dispersion where the speed of water can be approximated as $v_W \simeq q/m_W$. One can thus approximate water eigenstates as single plane waves with wavevector q. We also note that the water velocities experimentally reported by Secchi *et al.*[8] in larger CNTs were in the 10 μm/s range, which corresponds to very low q values (much smaller than $Q/2$, i.e., roughly corresponding to $10^{-6}Q$).

If no atomic or charge displacement occurs, the above-mentioned eigenstates remain unvaried during time evolution. Hence, one needs to overcome the Born–Oppenheimer approximation and further include electronic displacements in order to

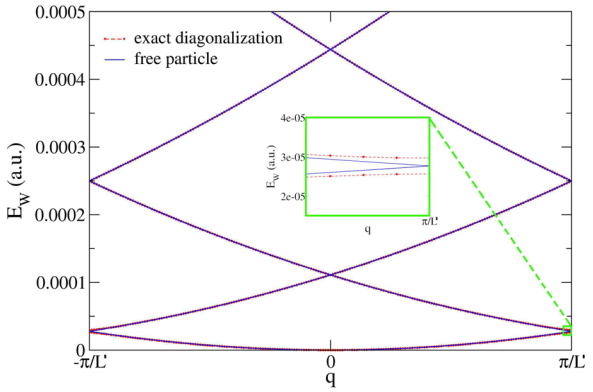

FIG. 2. Spectrum of the water molecule immersed in the (5,5) CNT potential. A comparison is given with the free-particle dispersion. Small deviations between the two spectra are found close to the BZ edges (details in the inset), where a slight gap opening is detected. Since the periodicity of the CNT potential is $L' = L/2$, the BZ is accordingly enlarged.

describe scattering processes. To account for vibrational and electronic degrees of freedom, one can Taylor-expand the potential energy V_W, starting from optimal ionic ($\tilde{\mathbf{R}}_{\mathbf{ion}}$) and electronic ($\boldsymbol{\delta\rho}_{\mathbf{el}} = 0$) configurations (Fig. 3).

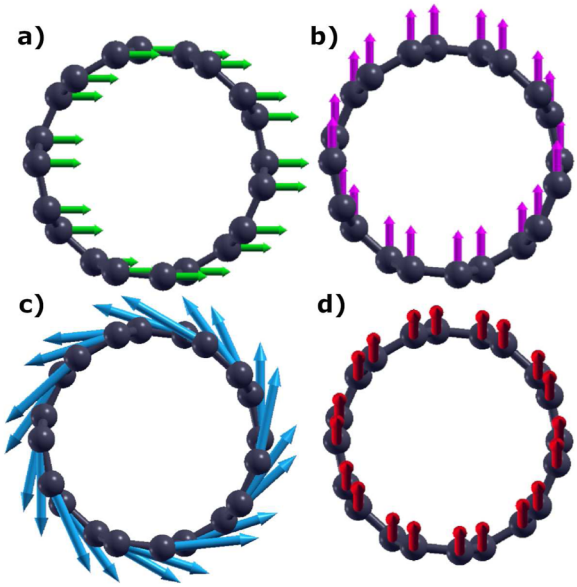

FIG. 3. (5,5) CNT: low-lying phonon modes, with linear dispersion close to $q = 0$. Colored arrows indicate the atomic displacement for the corresponding modes. (a) and (b) Are two degenerate transverse acoustic (TA) modes; (c) is the "twist" acoustic (TW) mode; and (d) is the longitudinal acoustic (LA) mode.

IV. PHONON EXCITATIONS

We introduce here a first-order Taylor expansion of V_W in the ionic displacements, defined as $\boldsymbol{\delta R}_{\text{ion}} = \mathbf{R}_{\mathbf{ion}} - \tilde{\mathbf{R}}_{\mathbf{ion}}$,

$$\begin{aligned} V_W(x_W, \mathbf{R}_{\mathbf{ion}}, \boldsymbol{\delta\rho}_{\text{el}} = 0) = V_W(x_W, \tilde{\mathbf{R}}_{\mathbf{ion}}, \boldsymbol{\delta\rho}_{\text{el}} = 0) \\ + \sum_i \partial_{R_{i,\text{ion}}} V_W\big(x_W, \mathbf{R}_{\mathbf{ion}}, \\ \times\ \boldsymbol{\delta\rho}_{\text{el}} = 0\big)\big|_{\mathbf{R}_{\text{ion}}=\tilde{\mathbf{R}}_{\mathbf{ion}}} \delta R_{i,\text{ion}} \\ + O(\delta R^2_{\text{ion}}). \end{aligned} \tag{2}$$

The potential derivatives can be written in terms of ionic forces, which can be straightforwardly computed by DFT: $\partial_{R_{i,\text{ion}}} V_W = -F_{i,\text{ion}}$; hence, the last term in Eq. (2) can be written in compact form as $-F_{i,\text{ion}}\delta R_{i,\text{ion}}$. Repeated indices are considered contracted from now on to simplify the notation (only in some specific cases will summations be explicited for clarity).

We now recall that when small atomic displacements from the CNT equilibrium geometry are considered, the CNT energy E_{CNT} (which could be obtained from DFT) can be approximated by a bilinear expression,

$$E_{\text{CNT}}(\mathbf{R}_{\mathbf{ion}}) = E_{\text{CNT},0} + \frac{1}{2} M_{i,j\text{CNT}} \delta R_{i,\text{ion}} \delta R_{j,\text{ion}} + O(\delta R^3_{\text{ion}}), \tag{3}$$

$$M_{i,j\text{CNT}} = \partial_{R_{i,\text{ion}}} \partial_{R_{j,\text{ion}}} E_{\text{CNT}}|_{\tilde{\mathbf{R}}_{\mathbf{ion}}}. \tag{4}$$

Diagonalization of $M_{i,j\text{CNT}}$ yields the collective vibrational modes (phonons). The geometry of these phonon modes in the CNT is expressed as $\delta\tilde{R}_j(q) = (1/\sqrt{N}) S^\dagger_{j,n} e^{iql_cL} \delta R_{l_c,n,\text{ion}}$, where the overall atomic index is now also split into an atomic index within the unit cell (n) and a cell index (l_c). Here, $S_{j,n}$ is a unitary matrix acting on unit cell coordinates, which determines the jth phonon geometry. As will be seen later, we will carry out our calculations by initially considering a box with finite length L_∞ and eventually taking the $L_\infty \to \infty$ limit. This box will contain N replicas of the CNT unit cell, and the N/L_∞ ratio will be kept constant.

Analogous transformations are also performed on $\mathbf{F}_{\text{ion}}$, so that $\tilde{F}_j(x_W, q) = (1/\sqrt{N}) S^\dagger_{j,n} e^{iql_cL} F_{n,l_c,\text{ion}}(x_W)$. After transforming to collective coordinates, the term $-F_{i,\text{ion}}\delta R_{i,\text{ion}}$ can be expressed as

$$\sum_{q=0}^{N-1} \tilde{F}_j(x_W, -q)\delta\tilde{R}_j(q). \tag{5}$$

Describing CNT phonons as quantum harmonic oscillators (QHO), the collective displacement operators can be finally rewritten in terms of QHO construction/annihilation operators,

$$\delta\tilde{R}_j(q) = (\tilde{a}_{j,q,\text{ion}} + \tilde{a}^\dagger_{j,q,\text{ion}})/(2m_C\omega_j(q))^{1/2}, \tag{6}$$

where $\omega_j(q)$ is the jth phonon frequency at wavevector q, and m_C is the C mass. Due to the ability to excite phonons, the term (5) provides a coupling between water and the CNT lattice and enables energy transfer between the two.

V. LOW-FREQUENCY PHONON MODES

Since we are interested in low-momentum water eigenstates (corresponding to the low water speeds measured experimentally),

energy transfers associated with friction should be accordingly small. Hence, only low-frequency acoustic phonon modes will be explored, while more energetic phonons will be discarded. In the (5,5) CNT, one encounters four acoustic modes[29,30] with vanishing frequencies in the $q \to 0$ limit. These are the transverse acoustic (TA) modes, which are doubly degenerate, a "twist" mode (TW), and the longitudinal acoustic mode (LA). We note that in the $q \to 0$ regime, the dispersion of these modes is linear, so one can mathematically describe the spectra as $\omega_j(q) = v_j q$, where the index j labels the specific phonon mode and the parameters v_j have the dimensions of a velocity. From reported phonon spectra,[30] we estimate the phonon velocities: $v_{\mathrm{TA}} = 4.5 \times 10^{-3}$a.u., $v_{\mathrm{TW}} = 6.9 \times 10^{-3}$a.u., and $v_{\mathrm{LA}} = 9.7 \times 10^{-3}$a.u., in fair agreement with similar nanotubes.[29] The geometries of these modes are reported in the literature[29] and correspond to transversal ionic shifts along the two directions $\hat{y}$ and $\hat{z}$ perpendicular to the CNT axis (TA), tangential atom displacements (TW; i.e., orthogonal to the CNT radius), and longitudinal $\hat{x}$ displacements (LA). Deviations from linearity close to the BZ edge are irrelevant to the present study and can be neglected.

VI. WATER–PHONON SCATTERING

We build upon our previous work,[15] adopting Fermi's golden rule description of the scattering between water and CNT phonons. Here, we will also explicitly integrate over reciprocal space, thereby accounting for phonon dispersion. Fermi's golden rule provides a simple expression for the computation of transition rates. A water molecule with initial wavevector $k_{\mathrm{W,i}}$ interacts with phonons via the coupling term given in Eq. (2) and is projected onto a final state with wavevector $k_{\mathrm{W,f}}$. The transition rate is accordingly expressed as

$$\Gamma^{\mathrm{ph}}_{\mathrm{i-f}} = 2\pi \left| \langle k_{\mathrm{W,f}}| - F^{\dagger}_{i,\mathrm{ion}} |k_{\mathrm{W,i}}\rangle \langle 1_{j,q}|\delta R_{i,\mathrm{ion}}|0_{j,q}\rangle \right|^2 \times \delta(E_{\mathrm{i,W}} - E_{\mathrm{f,W}} - \omega_j(q)), \tag{7}$$

where $|0_{j,q}\rangle$, $|1_{j,q}\rangle$ are the groundstate and first excited state relative to the jth phonon with wavevector q, while we recall that all repeated indices are contracted. The delta function enforces energy conservation, namely that the energy lost by water must correspond to that gained by phonon excitations. Here, we implicitly assume that the CNT initially occupies the phononic ground state. However, this assumption causes no loss of generality since excitation energies do not depend on the initial state in QHOs.

We make use of the collective coordinates [see Eqs. (5) and (6)] and further consider that when the jth phonon with wavevector q_{ph} is excited, one has $\langle 1_{j,q}|\tilde{a}^{\dagger}_{j,q}|0_{j,q}\rangle = 1$. Taking this into account, the term within the modulus in Eq. (7) becomes

$$\frac{1}{L_\infty \sqrt{N}} \int_{-L_\infty/2}^{L_\infty/2} dx_{\mathrm{W}} e^{i\Delta k_{\mathrm{W}} x_{\mathrm{W}}} \sum_n \sum_{q\in BZ} \sum_{l_c=0}^{N-1} F_{0,n}(x_{\mathrm{W}} - l_c L) \times S^{\dagger}_{j,n} e^{-iq(l_c L)} \frac{1}{\sqrt{2\omega_j(q) m_{\mathrm{C}}}}, \tag{8}$$

where $\Delta k_{\mathrm{W}} = k_{\mathrm{i,W}} - k_{\mathrm{f,W}}$ (summations were explicited in this case for clarity, and q is compatible with the chosen box). Since plane waves are non-normalizable in infinite space, we restricted x_{W} over the finite interval $[-L_\infty/2; L_\infty/2]$, as previously mentioned, eventually taking $L_\infty \to \infty$. Since a finite number of unit cell replicas (N) is contained in the box, we also impose that a finite water density is present in the CNT, namely that N' molecules are present within L_∞ (all water molecules have the same momentum for simplicity). We also note that $F_{n,l_c,\mathrm{ion}}$ can be Fourier transformed (in the infinite box limit) as $F_{n,l_c,\mathrm{ion}}(x_{\mathrm{W}}) = \frac{1}{2\pi}\int dq \tilde{f}_n(q) e^{iq(x_{\mathrm{W}} - l_c L)}$, where lattice periodicity is taken into account. After integration and recalling that $\sum_{l_c=0}^{N-1} e^{iql_cL} = N\delta_{q+mQ}$ (with m as an integer), Eq. (8) finally reduces to

$$\Gamma^{\mathrm{ph}}_{\mathrm{i-f}} = 2\pi \frac{N'}{NL^2} \left| \tilde{f}_n(\Delta k_{\mathrm{W}}) S_{n,j} \frac{1}{\sqrt{2\omega_j(\Delta k_{\mathrm{W}} + mQ) m_{\mathrm{C}}}} \right|^2 \times \delta(E_{\mathrm{i,W}} - E_{\mathrm{f,W}} - \omega_j(q)). \tag{9}$$

Taking the $L_\infty \to \infty$ limit, the ratios N/L_∞ and N'/N are kept constant while excited phonon states are traced. In deriving the above-mentioned equation, one finds that, in addition to energy conservation, one also needs to conserve crystal momentum. In fact, one has $k_{\mathrm{i,W}} = k_{\mathrm{f,W}} + q + mQ$, where m is an integer number. Since momentum conservation holds up to integer multiples of Q, our approach incorporates Umklapp processes.

At low $k_{\mathrm{i,W}}$, we approximate the energy spectrum of water as free-particle dispersion (as justified earlier). Hence, energy conservation can be expressed as

$$\frac{k^2_{\mathrm{i,W}} - k^2_{\mathrm{f,W}}}{2m_{\mathrm{W}}} = \omega_j(q). \tag{10}$$

Recalling that $k_{\mathrm{f,W}} = k_{\mathrm{i,W}} - q - mQ$, the above-mentioned equation yields a relation between the initial water speed $v_{\mathrm{i,W}} = k_{\mathrm{i,W}}/m_{\mathrm{W}}$, the phonon momentum q, and the parameter m,

$$v_{\mathrm{i,W}} = \frac{\omega_j(q)}{q + mQ} + \frac{q + mQ}{2m_{\mathrm{W}}}. \tag{11}$$

Considering that in the relevant low-momentum regime, the phonon dispersion is $\omega_j(q) = v_j q$, one can examine the different solutions that can be obtained by varying the integer parameter m. At $m = 0$, one has $v_{\mathrm{i,W}} \in [v_j, v_j + Q/2m_{\mathrm{W}}]$. The allowed speed interval drops down to $v_{\mathrm{i,W}} \in [Q/2m_{\mathrm{W}}, v_j/2 + Q/m_{\mathrm{W}}]$ for $m = 1$, and the lower extreme of the interval subsequently grows monotonically at higher m. This implies that scattering is only permitted when $v_{\mathrm{i,W}} > Q/2m_{\mathrm{W}}$, i.e., above ~50 m/s. The water molecule in the CNT will accordingly experience finite friction forces only when exceeding this critical velocity threshold.

Notably, the whole mechanism presents striking analogies with superfluidity.[34] In fact, a particle moving through a conventional superfluid also experiences vanishing friction below a critical velocity due to the incompatibility between energy and momentum conservation. In the present case, the CNT acts as an effective superfluid medium due to the quasi-linearity of its phononic and plasmonic excitation spectrum.

We note that a straightforward estimate of the thermal mean speeds in bulk water yields a value of a few hundred m/s, which exceeds the critical velocity threshold. This suggests that thermal water molecules should be able to scatter against the CNT. On the other hand, energy losses are known to occur[35] at the CNT entrance,

which may effectively reduce water speeds and momentum fluctuations. Further investigations are accordingly required in order to determine the exact water speed distribution in narrow CNTs at room temperature.

At high momenta, multiple solutions can be found, as reported in Fig. 4 for $m = 0, 1, 2, 3$, which could imply higher scattering rates. The need to numerically estimate the Fourier-transformed interaction from DFT calculations implies that numerical noise is unavoidably introduced in the present calculation. The computed water–phonon scattering rates thus provide a semi-quantitative estimate of the magnitude rather than accurate benchmark solutions.

VII. PLASMON EXCITATIONS

The approach followed so far for phonon excitations can be extended to plasmon modes, which are believed[12,16] to provide the leading friction contribution at the quantum mechanical level. In order to access the low-frequency plasmon spectrum, we adopt a discretized effective RPA theory. When an electric potential ϕ_j is applied to the atomic site $\mathbf{R}_{j,ion}$, the electronic charge at the atomic site i varies according to the relation $\delta\rho_i = \chi_{ij}\phi_j$, where χ_{ij} is the (discretized) density–density susceptibility. Following Ref. 31, we approximate the bare density–density response function by nearest-neighbor terms $\chi^0_{ij} = B\omega^{-2}(\delta_{ij} - 1/3h_{ij})$, where $h_{ij} = 1$ if i and j are nearest neighbors and 0 otherwise. This simple choice is proven[31] to predict the correct scaling for metallic systems in the $q \to 0$ limit. Although the bare response function is based on a nearest-neighbor hopping formalism, the interacting response eventually includes information about all interatomic Coulomb couplings and exhibits the correct long-range non-locality.

Since graphene[32] is well characterized and is the constituent material for CNT walls, we will extract the B parameter for a 2D graphene monolayer, subsequently accounting for the specific geometry of the (5,5) CNT within our discretized approach. In practice, the B parameter only controls the electron-hopping term, while the structure and topology of the CNT are included explicitly, determining the symmetry of the collective plasmon modes.

After the 2D Fourier transform, one obtains the $q \to 0$ limit

$$\tilde{\chi}^0_{\mathrm{G}}(\mathbf{q}) = \frac{Bq^2}{6\sqrt{3}\omega^2}. \tag{12}$$

From this expression for the bare susceptibility of graphene, one obtains the RPA interacting response $\tilde{\chi}^{\mathrm{RPA}}_{\mathrm{G}} = \tilde{\chi}^0_{\mathrm{G}}(1 - \tilde{\chi}^0_{\mathrm{G}}\tilde{v}_{2\mathrm{D}})$, where $\tilde{v}_{2\mathrm{D}}(q) = 2\pi/q$ is the 2D Fourier transformed Coulomb interaction. The poles of χ^{RPA} correspond to the plasmon frequencies, $\omega(q) = \sqrt{\pi Bq/(3\sqrt{3})}$. This expression should match the finite-temperature expression[33] for monolayer graphene,

$$\omega(q) = \sqrt{K_{\mathrm{B}}T4\ln(2)q}. \tag{13}$$

By direct comparison, one obtains $B = 12\sqrt{3}\ln(2)K_{\mathrm{B}}T/\pi$. The temperature will be fixed hereafter to $T = 300$ K, which is compatible with water flow.

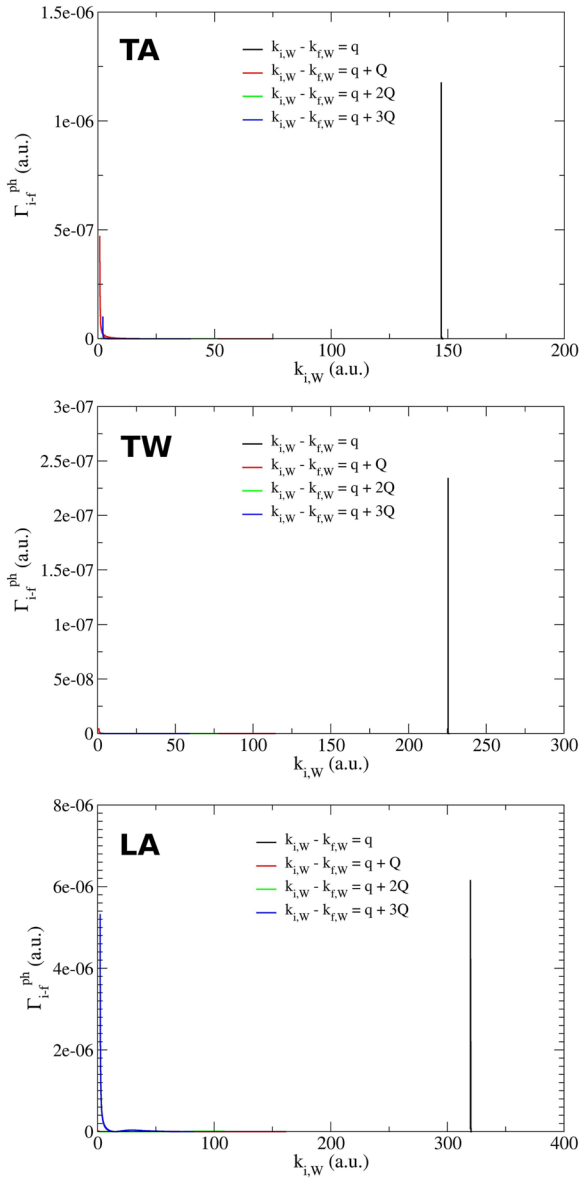

FIG. 4. Scattering rates, as defined in Eq. (8) for water–phonon scattering. N'/N is fixed to 22 (low water density). When $k_{i,W} < Q/2$, no scattering is permitted, so all curves start above this boundary. In practice, scattering is only allowed at high water speed. Components relative to the different phonon modes (TA, TW, and LA) and relative to different crystal momenta are reported separately for comparison. When momentum is strictly conserved (black lines), the permitted water momenta are extremely high. Lower $k_{i,W}$ (although still higher than $Q/2 \sim 0.7$ a.u.) is admitted when momentum is conserved up to integer multiples of Q. Given any $k_{i,W} > Q/2$, only a finite number of Q multiples are compatible with scattering.

Once the density response function is parameterized, one can write the RPA equations for the charge fluctuations,

$$\delta\rho_i = \chi^0_{ij}v(R_{i,\mathrm{ion}} - R_{j,\mathrm{ion}})\delta\rho_j, \tag{14}$$

where $v(R_{i,\mathrm{ion}} - R_{j,\mathrm{ion}})$ is the real-space Coulomb coupling between the ionic sites i and j, and χ^0_{ij} is the density response matrix for the CNT. Plasmons are computed as the self-sustaining charge fluctuation modes that satisfy

$$\left[\delta_{ij} - \chi^0_{ij} v(R_{i,\mathrm{ion}} - R_{j,\mathrm{ion}})\right]\delta\rho_j = 0. \tag{15}$$

Multiplying this equation by ω^2 and performing a Fourier transform, one obtains efficient numerical solutions for the plasmon spectrum. We note that the coupling between plasmons and localized electrons is neglected here since excitation of localized states is associated with much higher frequencies (of the order of 0.5 a.u.).

The Coulomb interaction $v(R_{i,\mathrm{ion}} - R_{j,\mathrm{ion}})$ can be expressed in matrix form as v_{ij}. Moreover, we can define $\chi'^0 = \chi^0\omega^2$. In matrix notation, the RPA equation becomes

$$(\chi'^0 v - \omega^2 \mathbb{I})\delta\rho_{\mathrm{el}} = 0. \tag{16}$$

Diagonalization of $\chi'^0 v$ can be made more efficient by matrix symmetrization. Here, χ'^0 is a Hermitian matrix and can be diagonalized by a transformation matrix O, $O^\dagger \chi'^0 O = \chi'^0_{\mathrm{diag}}$.

By rescaling the density displacements $\delta\rho$ as $\delta\rho' = O(\chi'^0_{\mathrm{diag}})^{-1/2} O^\dagger \delta\rho$, one rewrites the RPA Eq. (16) as

$$\omega^2 \mathbb{I}\delta\rho' = O(\chi'^0_{\mathrm{diag}})^{1/2} O^\dagger v O (\chi'^0_{\mathrm{diag}})^{1/2} O^\dagger \delta\rho'. \tag{17}$$

The eigenvalues of the Hermitian matrix $D_{\mathrm{pl}} = O(\chi'^0_{\mathrm{diag}})^{1/2} O^\dagger v O (\chi'^0_{\mathrm{diag}})^{1/2} O^\dagger$ correspond to the squared eigenfrequencies of the collective charge displacement modes (plasmons): $M^\dagger D_{\mathrm{pl}} M = \Omega_{\mathrm{pl}}$, where $\Omega_{\mathrm{pl},ij} = \delta_{ij}\omega^2_{\mathrm{pl},i}$. Here, the transformation matrix M accounts for the geometry of the corresponding eigenmodes.

Results reported in Fig. 5 indicate that the dispersion of the lowest band is quasi-linear at low momentum, in analogy to the phononic case. Other bands will be discarded due to their much higher energy, while the quasi-linear band could be fitted by $\omega_{\mathrm{pl}}(q) \sim v_{\mathrm{pl}} q$ when q is sufficiently small. The fitted velocity is $v_{\mathrm{pl}} \sim 0.3$a.u. (about two orders of magnitude higher than the phonon velocities). This result is in semi-quantitative agreement with recent[31] calculations.

We now note that the electrostatic energy due to charge displacements can be written as

$$U_{\mathrm{pl}} = \frac{1}{2}\delta\rho_i^\dagger v_{ij}\delta\rho_j. \tag{18}$$

After transformation, Eq. (18) reads (we drop indices for simplicity)

$$U_{\mathrm{pl}} = \frac{1}{2}\delta\rho'^\dagger M M^\dagger D_{\mathrm{pl}} M M^\dagger \delta\rho' = \frac{1}{2}\delta\rho'^\dagger M \Omega_{\mathrm{pl}} M^\dagger \delta\rho'. \tag{19}$$

This potential corresponds to that of a quantum harmonic oscillator with unitary mass and frequencies ω_i, while $M^\dagger\delta\rho' = M^\dagger O(\chi'^0_{\mathrm{diag}})^{-1/2} O^\dagger \delta\rho$ has the dimension of a length.

One can thus assume that the excitation of plasma modes can be effectively described by a QHO model (with unitary mass), associating creation $(a^\dagger_{i,\mathrm{pl}})$ and annihilation $(a_{i,\mathrm{pl}})$ operators to the plasmon mode as follows:

$$(M^\dagger\delta\rho')_i = \frac{(a_{i,\mathrm{pl}} + a^\dagger_{i,\mathrm{pl}})}{\sqrt{2\omega_i}}. \tag{20}$$

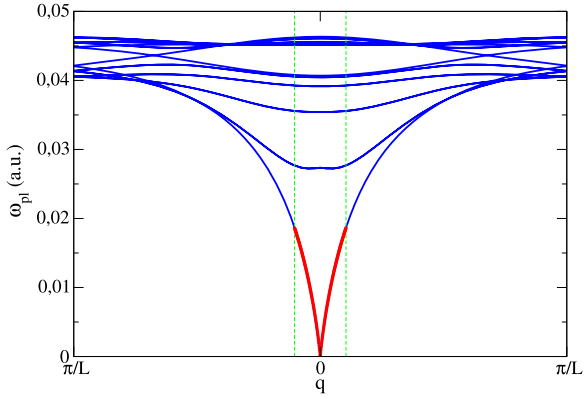

FIG. 5. Plasmon bands, obtained from the tight-binding model. Only the lowest band is taken into consideration in the computation of scattering rates, since very small energy transfer is expected from water. In the low-q regime (highlighted in red), the plasmon dispersion is approximately linear due to the quasi one-dimensionality of the metallic CNT.

VIII. WATER–PLASMON SCATTERING

We recall that water has a permanent dipole moment d_{W} (oriented along $\hat{x}$, with magnitude ~1.85 D), which interacts with the charge displacements occurring in the CNT via the Coulomb coupling v_{Coul}. Then, the water-charge coupling term

$$H_{\mathrm{w-c}} = d_{\mathrm{W}}\partial_{x_{\mathrm{W}}} v(\mathbf{R}_{\mathrm{W}} - \mathbf{R}_i)\delta\rho_i, \tag{21}$$

can be re-expressed as

$$H_{\mathrm{w-c}} = d_{\mathrm{W}}\partial_{x_{\mathrm{W}}} v(\mathbf{R}_{\mathrm{W}} - \mathbf{R}_i) O(\chi'^0_{\mathrm{diag}})^{1/2}_{ij} O^\dagger M_{jl} \frac{(a_{l,\mathrm{pl}} + a^\dagger_{l,\mathrm{pl}})}{\sqrt{2\omega_l}}. \tag{22}$$

Here we will only account for the lowest-energy plasmon mode, with quasi-linear dispersion at $q \to 0$, so that the index l will only run over this mode throughout the BZ. At a fixed q, the plasmon mode can be expressed as

$$\delta\tilde{\rho}_{\mathrm{pl}}(q) = (1/\sqrt{N})(M^{q\dagger} O^q (\chi'^{q,0}_{\mathrm{diag}})^{-1/2} O^{q\dagger})_{l_c,n} e^{iql_cL}\delta\rho_{l_c,n}, \tag{23}$$

where the overall atomic index is split, as before, into atomic index within the unit cell (n) and cell index (l_c), while the mode index is omitted since only the first plasmon is kept into account (only q-dependence remains). Creation/annihilation operators $(\tilde{a}^\dagger_{q,\mathrm{pl}}, \tilde{a}_{q,\mathrm{pl}})$ can be associated with this plasmon mode at each q in the BZ, as shown in Eq. (20).

Making use of Fermi's golden rule, we write the transition rate as

$$\Gamma^{\mathrm{pl}}_{\mathrm{i-f}} = 2\pi|\langle k_{\mathrm{W},f}|d_w(\partial_{x_{\mathrm{W}}} v) O^q (\chi'^{q,0}_{\mathrm{diag}})^{1/2} O^{q\dagger} M^q |k_{\mathrm{W},i}\rangle \times \langle 1_q|\frac{(\tilde{a}_{q,\mathrm{pl}} + \tilde{a}^\dagger_{q,\mathrm{pl}})}{\sqrt{2\omega_1(q)}}|0_q\rangle|^2 \delta(E_{\mathrm{W,i}} - E_{\mathrm{W,f}} - \omega_1). \tag{24}$$

The delta function enforces energy conservation, so that the energy lost by the water molecule should be transferred to the plasmon mode. One has to sum up all plasma states compatible with

the transition within the BZ. In order to compute $\Gamma^{\mathrm{pl}}_{\mathrm{i-f}}$, one needs to evaluate the squared modulus of the following integral:

$$\frac{d_{\mathrm{W}}}{\sqrt{N}L_\infty}\sum_{i,j}\int_{-L_\infty/2}^{L_\infty/2} dx_{\mathrm{W}} e^{i\Delta k_{\mathrm{W}} x_{\mathrm{W}}} \sum_{q\in BZ} \times \sum_{l_c=0}^{N-1} \partial_{x_{\mathrm{W}}} v(\mathbf{R}_{\mathrm{W}} - \mathbf{R}_i - l_c L\hat{x}) e^{-iql_c L} (\chi'^{q})^{1/2}_{ij} M^{q}_{j1} \frac{1}{\sqrt{2\omega_1(q)}}.$$

In addition, in this case, the summations over q and l_c were explicited for clarity. Contracted indices i, j are restricted to the unit cell, while q must again be compatible with the adopted box. The Coulomb interaction can be Fourier-transformed (in the infinite-length limit) as

$$v(\mathbf{R}_{\mathrm{W}} - \mathbf{R}_i - l_c L\hat{x}) = \frac{1}{2\pi}\int dq' 2K^0(q' R_i^{\perp}) e^{iq'(x_{\mathrm{W}} - x_i - l_c L)}, \quad (25)$$

where $R_i^{\perp}$ is the modulus of the component of R_i orthogonal to $\hat{x}$, while x_i is the $\hat{x}$ component. The scattering rate can thus be re-expressed after integration as

$$\Gamma^{\mathrm{pl}}_{\mathrm{i-f}} = \frac{N'2\pi}{NL^2}\left| d_{\mathrm{W}}\, i\Delta k_{\mathrm{W}} 2K^0(\Delta k_{\mathrm{W}} R_n^{\perp})\, e^{-i(k_{\mathrm{W}}+nQ)x_n} \times (\chi'^{\Delta k_{\mathrm{W}}+nQ})^{1/2}_{nj} M^{\Delta k_{\mathrm{W}}+nQ}_{j1} \frac{1}{\sqrt{2\omega_1(\Delta k_{\mathrm{W}}+nQ)}} \right|^2 \times \delta(E_{\mathrm{W,i}} - E_{\mathrm{W,f}} - \omega_1). \quad (26)$$

In addition, in this case, space integration/summation over unit cell replicas ensures the conservation of crystal momentum, $q = \Delta k_{\mathrm{W}} + nQ$.

Simultaneous conservation of energy and crystal momentum strongly restricts the number of permitted scattering processes, in analogy to the phonon case. To better understand this point, one can again approximate the spectrum of water by the free particle spectrum $E_{\mathrm{W}}(k) = k^2/(2m_{\mathrm{W}})$. At the same time, the plasmon dispersion close to $q \to 0$ can be reasonably well approximated as $\omega_{\mathrm{pl}}(q) \sim v_{\mathrm{pl}} q$. The ensuing constraint on water speeds is thus formally analogous to the phononic case,

$$v_{i,\mathrm{W}} = \frac{v_{\mathrm{pl}} q}{q + mQ} + \frac{q + mQ}{2m_{\mathrm{W}}}. \quad (27)$$

Our theory thus predicts that both phonon and plasmon excitations are effectively forbidden at low water speed. When water speeds exceed $Q/(2m_{\mathrm{W}})$, instead, a finite number of scattering processes (where momentum is shifted by different multiples of Q) are allowed. As shown in Fig. 6, momentum transfer by multiples of Q is heavily suppressed due to the fast decay of the Fourier-transformed Coulomb interaction. Meanwhile, high v_{pl} implies that scattering with momentum conservation can only occur at large water speeds.

By comparison with phononic scattering rates, we thus evince that, above the speed threshold, phonon modes contribute at larger rates to the overall scattering, while plasmonic effects become dominant at very high $k_{i,\mathrm{W}}$. Both plasmonic and phononic excitations should thus be taken into account in order to account for the different momentum regimes.

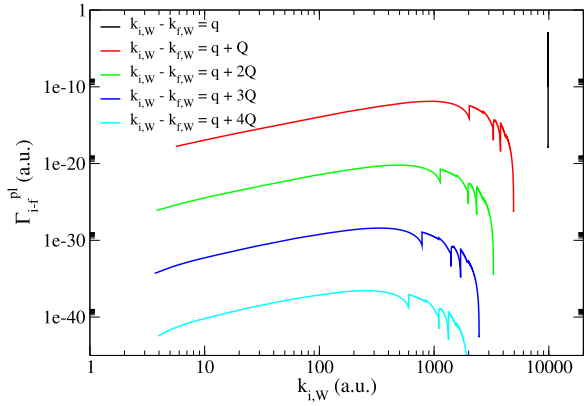

FIG. 6. Scattering rates, as defined in Eq. (26) for water–plasmon scattering. N'/N is fixed to 22 (low water density). Below $Q/2$, no scattering is permitted, like in the phononic case. In practice, scattering is only allowed at very high water speed. Components relative to different crystal momenta are reported separately for comparison. When momentum is strictly conserved (black lines), the permitted water momenta become even higher than in the phononic case due to the larger plasma frequencies (high v_{pl}). Corrugations in the curves indicate band crossing and are outside the expected linear dispersion range. Scattering with the transfer of multiple Q is suppressed due to the fast decay of the Fourier-transformed Coulomb coupling.

We also note that heavily non-linear plasmon and phonon modes can also moderately contribute at $k_{i,\mathrm{W}} > Q/2$, as already considered[15] in our previous work.

IX. DISCUSSION

The present treatment, based on a single water molecule, is valid in the low-density limit, where the energy scale of water–water interactions is much smaller than the water–CNT energy transfer. A more complete description of water–water interactions in the narrow (5,5) CNT would either require the introduction of correlated many-body wavefunctions or a perturbative approach. This would enable the description of water flow at higher density regimes, which are certainly relevant from an experimental point of view and will be the subject of future investigations.

Water–water couplings may store a certain amount of energy, but convergence tests[15] indicate a minor sensitivity of the water–CNT potential to the water–water coupling.

We also note that in the (5,5) CNT, only a single water molecule can be accommodated within the CNT transverse section. Conversely, in larger CNTs, collective mechanisms are expected to acquire higher relevance. In the vanishing curvature limit, water flow should eventually follow the quantum mechanical description proposed[12,16] for flat systems.

In the macroscopic limit, water molecules are known to exhibit non-trivial radial velocity profiles, and water–water interactions could participate in dissipation effects. The connection between ballistic flow and classical flow regimes at growing CNT radii can depend on a combination of mechanisms, such as thermalization and velocity distribution, which can enhance scattering amplitudes or dissipation effects emerging within the fluid. We also mention the abundance of low-energy degrees of freedom in water that can

couple with the CNT. We also note that larger CNTs are also characterized by softer vibrational modes that stem from the deformation of the CNT walls. Local density variations in water could contribute to these CNT deformations.

Since a wavepacket could provide a better description of a traveling water molecule, we explicitly consider the following superposition of plane waves:

$$|\phi_i\rangle = \sum_k C_k |k\rangle. \tag{28}$$

When willing to estimate the scattering probability into a final state $|k'\rangle$, one should compute the matrix elements

$$\sum_k C_k \langle k'|H'|k\rangle, \tag{29}$$

where H' is the interaction term, which can either represent water–phonon or water–plasmon couplings. These matrix elements, already computed earlier, enable a straightforward estimate of scattering rates.

We note that CNTs were proposed as an effective means for the development of energy-efficient water filtration[11,12] devices that could effectively contrast increasingly severe shortages of clean-water supplies. Highly efficient CNT membranes were already fabricated[6] by parallel stacks of CNTs immersed in a silicon nitride matrix. Other potential nanofluidic applications include minimally invasive and non-destructive injections through cellular membranes or water delivery in artificial photosynthetic[36] systems.

X. CONCLUSIONS

In conclusion, we provided a fully quantum mechanical description of the scattering that arises when a water molecule flows through a narrow (5,5) CNT. This scattering is ultimately responsible for the friction force experienced by flowing water, as it effectively implies energy-transfer from water to the CNT. Both phononic and plasmonic degrees of freedom in the CNT are taken into account by means of Fermi's golden rule, while the necessary parameters are obtained by first-principle density functional theory calculations. We find that water can scatter against the CNT only when its speed exceeds a critical value of ~50 m/s, which provides a relevant extension of conventional superfluidity to standard CNTs. Here, the critical speed is smaller than the average thermal velocity of bulk water at room temperature. Hence, further analysis is demanded in order to precisely assess the water-speed distribution in sub-nanometer CNTs and to fully characterize the actual flow regime. When scattering takes place, only a limited number of final states are available, and scattering rates remain small. Phonon scattering dominates at lower momentum transfers, while plasmon contributions dominate at larger momenta. Both degrees of freedom should be accordingly taken into account.

ACKNOWLEDGMENTS

A.A. and P.L.S. acknowledge funding from Cassa di Risparmio di Padova e Rovigo (CARIPARO)—grant EngvdW. A.A. acknowledges funding from Cassa di Risparmio di Padova e Rovigo (CARIPARO)—grant Synergy. A.A. acknowledges funding from the physics and astronomy department of the University of Padova (PARD grant).

AUTHOR DECLARATIONS

Conflict of Interest

The authors have no conflicts to disclose.

Author Contributions

Alberto Ambrosetti: Conceptualization (lead); Data curation (lead); Formal analysis (lead); Funding acquisition (equal); Investigation (lead); Methodology (lead); Project administration (equal); Resources (equal); Software (lead); Supervision (lead); Validation (lead); Visualization (lead); Writing – original draft (lead); Writing – review & editing (lead). **Pier Luigi Silvestrelli**: Conceptualization (supporting); Data curation (supporting); Formal analysis (supporting); Funding acquisition (equal); Investigation (supporting); Methodology (supporting); Project administration (equal); Resources (equal); Software (supporting); Supervision (supporting); Validation (supporting); Visualization (supporting); Writing – original draft (supporting); Writing – review & editing (supporting).

DATA AVAILABILITY

The data that supports the findings of this study are available within the article.

REFERENCES

[1] R. B. Bird, W. E. Stewart, and E. N. Lightfoot, *Transport Phenomena*, 2nd ed. (Wiley, New York, 2005).
[2] C. Zhu *et al.*, Proc. Natl. Acad. Sci. U. S. A. **116**, 16723–16728 (2019).
[3] A. Ambrosetti, F. Ancilotto, and P. L. Silvestrelli, J. Phys. Chem. C **117**, 321–325 (2013).
[4] K. Falk, F. Sedlmeier, L. Joly, R. R. Netz, and L. Bocquet, Nano Lett. **10**, 4067–4073 (2010).
[5] M. Majumder, N. Chopra, R. Andrews, and B. J. Hinds, Nature **438**, 44 (2005).
[6] J. K. Holt, H. G. Park, Y. Wang, M. Stadermann, A. B. Artyukhin, C. P. Grigoropoulos *et al.*, Science **312**, 1034–1037 (2006).
[7] M. Whitby, L. Cagnon, M. Thanou, and N. Quirke, Nano Lett. **8**, 2632–2637 (2008).
[8] E. Secchi, S. Marbach, A. Nigués, D. Stein, A. Siria, and L. Bocquet, Nature **537**, 210 (2016).
[9] D. Mattia and F. Calabró, Microfluid. Nanofluid. **13**, 125–130 (2012).
[10] S. K. Kannam, B. D. Todd, J. S. Hansen, and P. J. Daivis, J. Chem. Phys. **138**, 094701 (2013).
[11] A. Kalra, S. Garde, and G. Hummer, Proc. Natl. Acad. Sci. U. S. A. **100**, 10175–10180 (2003).
[12] B. Fraser, Nature **573**, 171–172 (2019).
[13] G. Hummer, J. C. Rasaiah, and J. P. Noworyta, Nature **414**, 188–190 (2001).
[14] S. Joseph and N. R. Aluru, Nano Lett. **8**, 452–458 (2008).
[15] A. Ambrosetti, G. Palermo, and P. L. Silvestrelli, J. Phys. Chem. C **126**, 20174–20182 (2022).
[16] N. Kavokine, M.-L. Bocquet, and L. Bocquet, Nature **602**, 84–90 (2022).

[17]A. T. Bui, F. L. Thiemann, A. Michaelides, and S. J. Cox, Nano Lett. **23**, 580–587 (2023).
[18]A. Ambrosetti and P. L. Silvestrelli, Carbon **139**, 486–491 (2018).
[19]A. Ambrosetti and P. L. Silvestrelli, J. Phys. Chem. Lett. **10**, 2044–2050 (2019).
[20]A. Ambrosetti, N. Ferri, R. A. DiStasio, Jr., and A. Tkatchenko, Science **351**, 1171–1176 (2016).
[21]P. Giannozzi, S. Baroni, N. Bonini, M. Calandra, R. Car, C. Cavazzoni *et al.*, J. Phys.: Condens. Matter **21**, 395502 (2009).
[22]J. P. Perdew, K. Burke, and M. Ernzerhof, Phys. Rev. Lett. **77**, 3865 (1996).
[23]M. Ricci, P. L. Silvestrelli, J. F. Dobson, and A. Ambrosetti, J. Phys. Chem. Lett. **13**, 8298–8304 (2022).
[24]A. Ambrosetti, A. M. Reilly, R. A. DiStasio, Jr., and A. Tkatchenko, J. Chem. Phys. **140**, 18A508 (2014).
[25]A. Tkatchenko, A. Ambrosetti, and R. A. DiStasio, Jr., J. Chem. Phys. **138**, 074106 (2013).
[26]A. Ambrosetti, P. Umari, P. L. Silvestrelli, J. Elliott, and A. Tkatchenko, Nat. Commun. **13**, 813 (2022).
[27]S. Grimme, J. Comput. Chem. **27**, 1787–1799 (2006).
[28]P. Hauseux, A. Ambrosetti, S. P. A. Bordas, and A. Tkatchenko, Phys. Rev. Lett. **128**, 106101 (2022).
[29]M. S. Dresselhaus and P. C. Eklund, Adv. Phys. **49**, 705–814 (2000).
[30]H. W. Zhang, Z. Yao, J. B. Wang, and W. X. Zhong, Int. J. Solids Struct. **44**, 6428–6449 (2007).
[31]J. Dobson and A. Ambrosetti, J. Chem. Theory Comput. **19**, 6434–6451 (2023).
[32]A. Geim and K. S. Novoselov, Nat. Mater. **6**, 183–191 (2007).
[33]G. Gomez-Santos, Phys. Rev. B **80**, 245424 (2009).
[34]A. Ambrosetti, P. L. Silvestrelli, and L. Salasnich, Phys. Rev. Lett. **131**, 206301 (2023).
[35]F. Ebrahimi, F. Ramazani, and M. Sahimi, Sci. Rep. **8**, 7752 (2018).
[36]D. K. Dogutan and D. G. Nocera, Acc. Chem. Res. **52**, 3143–3148 (2019).